Journal of Qassim University for Science
2024, *Vol 3* (Issue 1), pp. 157-176
Received: 15 February 2024
Revised: 15 March 2024
Accepted: 30 March 2024

JQUS

High dielectric and conduction proprieties of Na^+doped lanthanum Strontium manganite for cathode materials application.

Rahma Ayed Brahem
Department of Physics, College of Science, Qassim University, Buraidah, 51452, Saudi Arabia
, E-mail R.brahem@qu.edu.sa

Abstract: In the present work, the mixed valence $La_{0.7}Sr_{0.2}Na_{0.1}MnO_3$ manganite is elaborated using the sol-gel preparation route. The structural, electrical, and dielectric properties of the $La_{0.7}Sr_{0.2}Na_{0.1}MnO_3$ are detailed over broad temperature and frequency ranges to get information about the dynamic of the charge carriers in such a manganite structure. At room temperature, combinations of the experimental X-ray diffraction (XRD) measurements and the calculation results using the Rietveld analysis reveal that $La_{0.7}Sr_{0.2}Na_{0.1}MnO_3$ crystallizes in a pure phase belonging to the rhombohedral structure with $R\bar{3}c$ space group. Using the Size-Strain technique, the estimated crystallite sizes and lattice strain values are D_{SSP}=24 nm and ε_{SSP} =2.2.10^{-3}, respectively. The electrical DC conductivity investigation reveals that the studied material exhibits a semiconductor behavior over the explored temperature range. Such behavior is investigated using the small polaron and the variable range hopping conduction models.

Moreover, the DC conductivity study shows that the presence of significant charge mobility and strong electron-phonon interactions characterizes La0.7Sr0.2Na0.1MnO3. For the studied system, the deduced Debye temperature is θ_D=520 K. The presence of the Na^+ cation in the studied manganite has improved mainly the electrical DC conductivity value especially at around room temperature that reaches σ_{DC} (300K) = 4.3 10^{-2} $S.cm^{-1}$. A quantitative investigation of the temperature dependence of the frequency exponents n (T) at high frequencies reveals that the Correlated Barrier Hopping model overpowered the electrical conduction in the AC regime. The scaling exponent (α) proves the validity of the time-temperature superposition principle. According to Koop's theory, the frequency dependence of the dielectric constant (ε'') response is attributed to the chemical micro-heterogeneity and the interfacial polarization effects. Furthermore, the colossal behavior of the dielectric constant (ε'') with a value over 10^6 and the presence of high electrical conductivities of 4.3 10^{-2} $S.cm^{-1}$ denote a possible application of this compound in energy storage devices.

.

Keywords: Electrical conductivity; Hopping process; Dielectric constant; Perovskite; X-ray diffraction (XRD)..

1. INTRODUCTION

Industrial and global economic development has tremendously increased over the last few years, inducing a high rate of total energy consumption worldwide **[1, 2]**. More than half of consumed energy is generated from nonrenewable natural sources that cause severe global environmental consequences. Therefore, exploiting renewable and clean energy sources such as solar, wind, or geothermal is the obvious solution to avoid these consequences **[3]**. Interesting and promising research for alternative sources poses a challenge for developing efficient and reliable energy storage processes, which presents a vital topic in nanotechnologies systems **[4]**. Several designs and research on green energy-storage systems have been developed with important tools for many electric devices and industrial sectors that have aroused extensive interest **[5]**. The performance assured all these kinds of technologies of the electrode materials related to the charge/discharge processes associated with the oxygen evolution/reduction reaction (OER / ORR) **[6]**. Numerous studies are focused today on developing new electrode materials such as metal oxides, conductive polymers, and functional carbon **[7]**. Particularly, perovskite-based lanthanum Strontium manganite ($LaSrMnO_3$) materials have emerged as an important family of functional nanomaterials for various industrial applications such as chemical energy storage devices and dielectric capacitors **[8]**.

Perovskite-based on the Lanthanum Strontium manganite oxide ($LaSrMnO_3$) is well known for its colossal magnetoresistance, ferromagnetic-paramagnetic transition, high magnetic interaction, and magnetocaloric properties that have been explained by various theoretical models and scientific reports **[9]**. However, the double exchange (DE) mechanism proposed by Zener is the most appropriate process applied to explain the conversion associated with the electron (hole) transfer between two partially filled d-shells, eg (Mn^{3+}) and t_{2g} (Mn^{4+}) **[10]**. This electron motion is governed and controlled by the strong on-site Hund's coupling and the dynamic Jahn-Teller (JT) distortions generated from a strong electron-phonon coupling **[11]**. This material has recently gained much attention as an efficient electrode used in several energy storage and conversion technologies. P. Muhammed Shafi et al. **[12]** report that substitution and tunable crystal symmetry can be an efficient solution to increase the performance of the conductivity and electrochemical mechanism. They argue that $La_{0.7}Sr_{0.3}Mn_{0.5}Fe_{0.5}O_3$ compound can be a good sample for electrochemical application with faradaic behavior. Moreover, Xueqin Lang et al. **[13]** studied the $La_{1-x}Sr_xMnO_3$ and proved its possible application as pseudo-capacitance electrode materials governed by the redox reaction of the cation intercalation. They also showed that $La_{1-x}Sr_xMnO_3$ presents a large specific surface and good electrical conductivity that have an important role in the electrode application.

The physical properties of manganite can be improved by several parameters such as synthesis methods, insertion of nanostructures, and substitution sites **[14]**. However, different reports denote that even a small amount can alter the physical properties through steric effects and lead to a modification of the Mn^{3+}/Mn^{4+} state **[15]**. Recently, new research on manganite with Na^+ doping indicates the coexistence of large magnetic and electrical properties that open the door to multiferroic compounds for nanomaterials application **[16]**. In addition, doping Na^+ is rarely investigated on electric and dielectric proprieties that have an important role in making information and analyses for suitable applications. Such observation motivated us to understand the transport properties and optimized physical parameters of $La_{0.7}Sr_{0.2}Na_{0.1}MnO_3$ with better stability using impedance spectroscopy for energy storage applications

2. EXPERIMENTAL

$La_{0.7}Sr_{0.2}Na_{0.1}MnO_3$ nanomaterials were elaborated by the sol-gel technique to produce a suitable ceramic with high quality and homogeneity. The high-purity nitrate precursors (obtained from Sigma Aldrich) La $(NO3)_3$, Sr $(NO3)_2$, $NaNO_3$, and Mn $(NO_3)_2$ were used as starting rows to elaborate the $La_{0.7}Sr_{0.2}Na_{0.1}MnO_3$ compound. The stoichiometric mixtures of metal nitrates weighed following the desired compositions were dissolved in distilled water. Slow evaporation was applied with a continuous stirring. Ethylene glycol (EG) and citric acid were added as chelating and polymerization agents, forming a stable solution with a pH scale range between 6.5 and 7. After obtaining a transparent solution, further heating under stirring was applied (between 150 and 180 °C) until the formation of a dry mixture. This dry mixture was calcined at 800 °C for 24h with intermediate regrinding and repelling. Afterward, black ash was pressed into pellets (8mm diameter and 6mm thickness) and sintered at 1000 °C for 12h. Finally, this sample was air-quenched to achieve a high-quality and homogeneous microstructure at the annealed temperature. To analyze the microstructural features of the sample and estimate the grain size value at room temperature, we used a scanning electron microscopy (SEM) instrument on a JSM-6400 apparatus under the applied voltage of 25 KV. Further, the structure and homogeneity of the sample were analyzed by the X-ray diffraction (XRD) method using a ‘‘Panalytical Xpert-Pro’’ diffractometer. The results of XRD Measurements were scanned using CuK_α radiation (λ=1.5406Å) under an angular range of $10° \leq 2\theta \leq 100$ by a 0.017° step-size. Rietveld process and FULLPROF software were used to fit the obtained patterns and to collect the structural parameters **[17]**.

For the electrical characterizations, two copper wires used as electrodes were connected to an Al-film (6 mm diameters and 200 nm thick) coated on each side of the pellets using a circular mask and thermal vapor deposition (TVP). However, the capacitance C and conductance G measurements were obtained over a wide range of frequencies (from 100 Hz to 1 MHz) using an Agilent 4294A analyzer coupled with a liquid nitrogen cryostat which allows the variation of temperature from 200K to 360K. All electrical data were registered in vacuum and dark.

3. RESULTS AND DISCUSSION.

3.2 STRUCTURAL CHARACTERIZATION AND MORPHOLOGICAL INFORMATION

The inset of **Fig.1** presents a surface of $La_{0.7}Sr_{0.2}Na_{0.1}MnO_3$ perovskite oxide using SEM micrographs. One can observe a densely packed microstructure exhibiting non-uniform morphology distribution and irregular repartition of distinct grain structure with spheroid-like behavior with unequal size separated by well-defined grain boundaries over the entire area. This inhomogeneous microstructure impedes the intrinsic properties of the compound related to the high current percolation and opens up the conduction channels process **[18, 19]**. Furthermore, a porous structure was noticed, which may be crucial in supplying the active area for the electrochemical reaction of the oxygen electrode. The grain size was estimated using Image. J software based on the linear intercept method and the obtained data were fitted by “Gaussian function” (Inset of **Fig.1).**

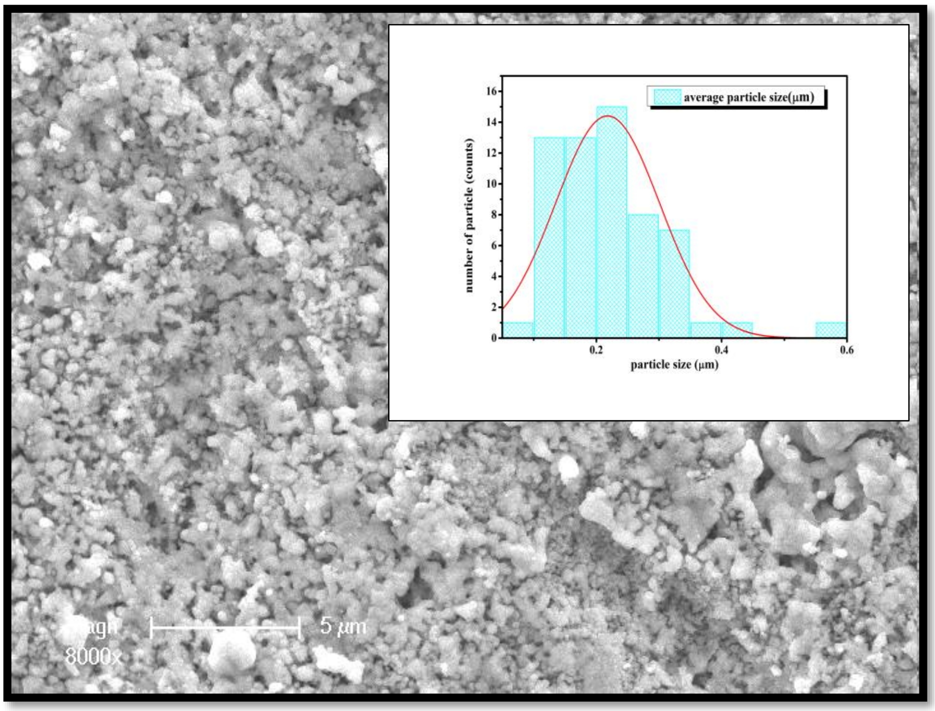

Fig. 1: SEM image for our $La_{0.7}Sr_{0.2}Na_{0.1}MnO_3$. The inset contains the histograms of the grain size distribution.

However, to examine the structural proprieties of the $La_{0.7}Sr_{0.2}Na_{0.1}MnO_3$ nano-powder, experimental XRD pattern data were recorded and analyzed employing the standard Rietveld method and FULLPROF software as shown in **Fig.2**.

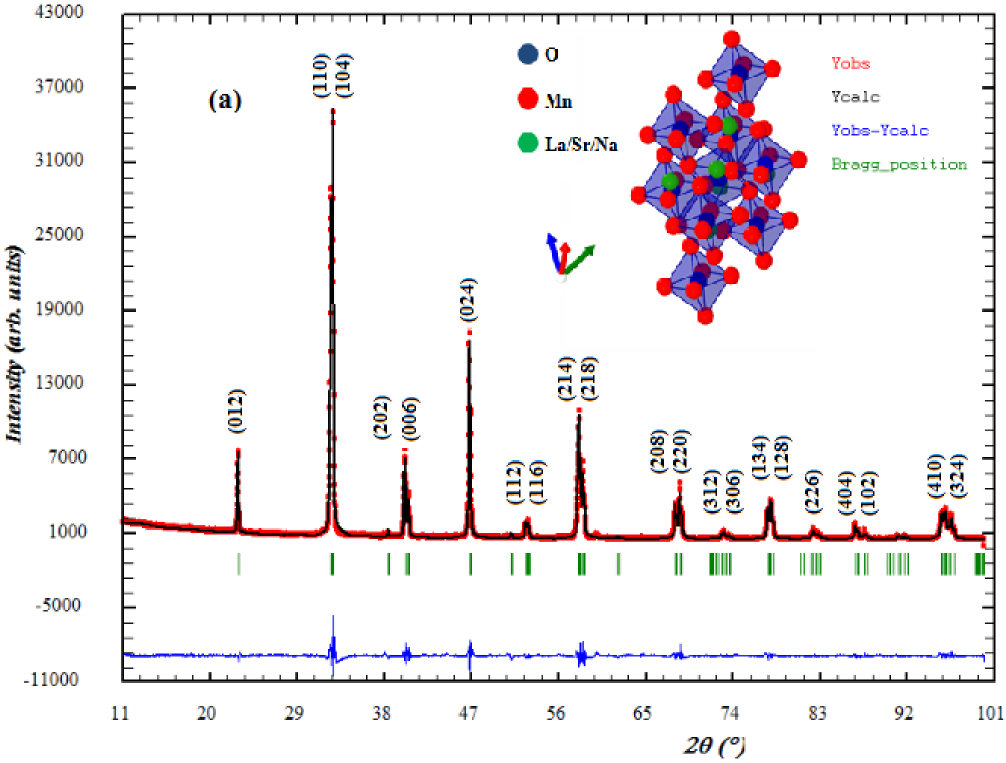

Fig. 2: Rietveld pattern determined from X-ray powder diffraction of the $La_{0.7}Sr_{0.2}Na_{0.1}MnO_3$ ceramic. Marks: experimental data; solid line: theoretical results. Vertical bars indicate Bragg reflection positions. The difference between experimental data and theoretical results is given by at the bottom. Inset: the crystal structure and the MnO_6 octahedron for our compound.

Obviously, sharp and intense features of the powder diffraction peaks confirm the presence of high crystalline structure without any kind of impurities. The refined profile revealed that all peaks can be indexed based on the rhombohedral unit cell (space group $R\bar{3}c$, No. 167). In this type of crystal symmetry, the standard Wyckoff position was used to estimate the initial parameters. (La, Sr, Na) atoms shared the A-site at 6a (0, 0, 1/4) positions and the Mn-site cations were randomly distributed at the 6b (0, 0, 0), meanwhile, the oxygen anions occupied 18e (x, 0, 1/4). The matching between the fitted and observed diffraction data was evaluated through the adequacy of the fit indicator χ^2 and the reliability R-factors (R_{wp}, $R_{w,}$ and R_e) reported in **Table 1**. This table summarizes the deduced results of structural refinement such as atomic coordinate, lattice parameters, bond angle ($< Mn - o - Mn >$), and unit cell volume (v).

Phase R$\bar{3}$C	
Structural model Cell parameters	
a(Å)	5.506 (5)
c(Å)	13.360 (2)
Cell volume (Å^3)	350.880 (1)
Isotropic thermal parameters	
B(La/Na/Sr) (Å^2)	0.98(5)
B(Mn/Ti) (Å^2)	0.94(2)
B(O) (Å^2)	0.96(3)
R factor	
R_{wp}(%)	11.2
R_B(%)	13.2
R_F (%)	6.7
χ^2	1.7
Bond lengths and Bond angles	
d_{Mn-O} Å	1.74 (3)
$\theta_{Mn-O-Mn}$	188.59 (2)
$<r_B>$Å	0.687 (6)

Table 1: Structural parameter and refinement results of X-ray diffraction data at room temperature for $La_{0.7}Sr_{0.2}Na_{0.1}MnO_3$ ceramics.

It is worth noting that the parameters of the hexagonal cell (a and c) and the unit cell volume slightly decreased with increasing Sodium amount **[20]**. This behavior can be explained by the size effect of the A- site related to the average ionic radius of Na^+ (1.39 Å) and Sr^{2+} (1.44 Å) **[21]**.

In addition, introducing Sodium element is accompanied by a partial conversion of the Mn^{3+} (0.65 Å) to Mn^{4+} (0.53 Å) following the formula $La_{0.7}Sr_{0.3-x}Na_xMn^{3+}_{0.7-x}Mn^{4+}_{0.3+x}O_3$. The cooperative process of the average A site radius and the increase of Mn^{4+} caused a change in the Mn-O-Mn angles and the Mn-O distances which in turn reduced the exchange interaction strength and affected the physical properties of the compounds **[22]**. This table also contains the average size $< r_A >$ and the mismatch size σ^2 of the A-site cations estimated using the values of ionic radii. Generally, the nature and type of electrical transport properties of the materials were attributed to the structural behavior and microstructural quality of ceramic. Usually, doped-monovalent element affects mainly the structural properties of manganite oxides and the strength of the DE mechanism related to the mixed valence Mn^{3+}/Mn^{4+} **[23]**.

To understand the regularities governing the formation of perovskite oxide systems and their structure stability, Goldschmidt defined an empirical tolerance factor (t_G) which depends heavily on the degree of cell distortion and the size of cations that fill the A and B sites. This factor can be estimated through the following equation **[24]**:

$$t_G = \frac{r_{(La,Sr,Na)} + r_O}{\sqrt{2}(r_{Mn} + r_O)} \qquad \textbf{(1)}$$

Where $r_{(La,\ Sr,\ Na)}$, $r_{Mn,}$ and r_O are the mean ionic radius of the different elements occupying the site A, B, and O sites in ABO_3, respectively.

Indeed, the stable crystal structure of a typical perovskite system appeared in the appropriate range of $0.75 < t_G < 1$ while an ideal symmetry was detected when the value of this factor tended to unit. Goldschmidt's factor defines the chemical insertion and distortion produced by the motion of cations into the ABO_3 structure compared to the ideal packing. However, the value of the tolerance factor is calculated using Shannon's ionic radius **[25]** and was found equal to 0.945. This result proves the stability of the rhombohedral structure and confirms the deviation of the Mn-O-Mn bond angle from 180°, which is consistent with the Rietveld refinement.

Based on the profile of the X-ray peak, several quantitative analysis methods and processes were applied to understand the crystal distortions, lattice mismatch, and imperfections of the nanoparticles. Debye-Scherrer technique is a well-known method that can be used to estimate the crystallite size D using the peak broadening process following expression **[26]**:

$$D = \frac{k\,\lambda}{\beta_S \cos\theta_{hkl}} \qquad \textbf{(2)}$$

Where *k* presents the shape factor, λ denotes the wavelength of Cu-K_α radiation, β_S is the integral breadth of the most intense peak (FWHM) and θ_{hkl} refers to Bragg's diffraction angle. Therefore, the expression of the integral breadth β_S equation can be obtained by rearranging **Eqs. (2)**:

$$\beta_S = \frac{k\,\lambda}{D\cos\theta_{hkl}} \qquad \textbf{(3)}$$

The lattice strain ε is also a very important parameter that reflects all structural distortions in the powder ceramic which can be defined by the Stokes-Wilson relation **[27]**:

$$\varepsilon = \frac{\beta_\varepsilon}{4\tan\theta_{hkl}} \qquad \textbf{(4)}$$

Where β_ε is the strain broadening and θ_{hkl} represents the diffraction angle.

However, the Williamson-Hall (W-H) method was induced to estimate the grain size and lattice effect based on the XRD peak broadening of the ceramics **[28]**. Williamson-Hall equations assume that the integral breadth β_{hkl} of the observed XRD line peaks is the addition of grain size (Scherrer) broadening β_S and strain broadening β_ε effect which can be expressed as:

$$\beta_{hkl} = \beta_\varepsilon + \beta_S \qquad \textbf{(5)}$$

Adding the value of β_S and β_ε into **Eqs.6**, we obtain:

$$\beta_{hkl} = 4\,\varepsilon \tan\theta_{hkl} + \frac{k\,\lambda}{D_{W-H}\cos\theta_{hkl}} \quad \textbf{(6)}$$

By rearranging **Eqs.6**:

$$\beta_{hkl}\cos\theta_{hkl} = 4\,\varepsilon \sin\theta_{hkl} + \frac{k\,\lambda}{D_{W-H}} \quad \textbf{(7)}$$

To calculate the grain size and lattice strain from the DRX profile, the W-H relation in **Eqs.7** can be simulated as the standard equation for a straight line (Y= AX+ B) by performing the $\beta_{hkl}\cos(\theta_{hkl})$ versus $4\sin\theta_{hkl}$ curve as shown in **Fig.3 (a).** From the regression line and linear fit, the crystallite size and the strain value were calculated from the y-intercept and the slope of the straight line, respectively.

Besides this method, Halder and Wagner (H-W) induced an alternative formula based on the deconvolution of XRD integral breadth using two parameters β_L and β_G described by a Lorentzian profile (L) and Gaussian profile (G) of grain size $D_{H\text{-}W}$ and lattice strain ε, respectively **[29]**.

$$\beta_{hkl}^2 = \beta_L \beta_{hkl} + \beta_G^2 \quad \textbf{(8)}$$

Where

$$\beta_L = \frac{K\lambda}{D\cos\theta_{hkl}} \quad \textbf{(9)}$$

$$\beta_G = 4\varepsilon \tan\theta_{hkl} \quad \textbf{(10)}$$

By transposing parameters in Eq. (8), we get:

$$\beta_{hkl} = \beta_L + \frac{\beta_G^2}{\beta_{hkl}} \quad \textbf{(11)}$$

Putting equations (9) and (10) in Eq. (11), we find:

$$\beta_{hkl} = \frac{K\lambda}{D_{H-W}\cos\theta_{hkl}} + \frac{16\varepsilon^2\tan^2\theta_{hkl}}{\beta_{hkl}} \quad \textbf{(12)}$$

Rearranging Eq. (12) and multiplying both sides by $cos\theta_{hkl}/\lambda$, we obtain:

$$\frac{\beta_{hkl}\cos\theta_{hkl}}{\lambda} = \frac{K}{D_{h-w}} + \varepsilon^2 \frac{16\sin^2\theta_{hkl}}{\beta_{hkl}\lambda\cos\theta_{hkl}} \quad \textbf{(13)}$$

If we suppose that $Y=\beta_{hkl}\cos\theta_{hkl}/\lambda$ and $X=16\sin^2\theta_{hkl}/(\beta_{hkl}\lambda\cos(\theta_{hkl}))$, Eq. (12) become:

$$Y = \frac{K}{D} + \varepsilon^2 X \quad \textbf{(14)}$$

drawing the variations of Y versus X, we obtain a linear curve where the lattice strain and crystallite size value are estimated using a linear fit to the data as shown in **Fig.3 (b).**

Recently, the size-strain plot (SSP) technique has been applied to estimate the crystallite size D_{SSP} and strain ε_{SSP} for the isotropic structure based on Lorentzian and Gaussian functions, respectively **[30]**. This method is given using the formula below:

$$(d\beta cos\theta)^2 = \frac{K}{D_{SSP}}(d^2\beta cos\theta) + (\frac{\varepsilon_{SSP}}{2})^2 \qquad \textbf{(15)}$$

Fig.3 (c) presents $(d\beta cos\theta)^2$ versus $(d^2\beta cos\theta)$ spectra of the $La_{0.7}Sr_{0.2}Na_{0.1}MnO_3$ compound. From the linear extrapolated data, D_{SSP} and ε_{SSP} were calculated from the slope and intercept, respectively.

The calculated values of lattice strain and average crystallite size using different methods are listed in **Table 2**. The obtained values of crystallite size estimated using W-H and SSP methods are slightly different and the SSP curve can give the most appropriate results of the microstructural parameters with more precision since the data more accurately fit in this method **[31, 32]**

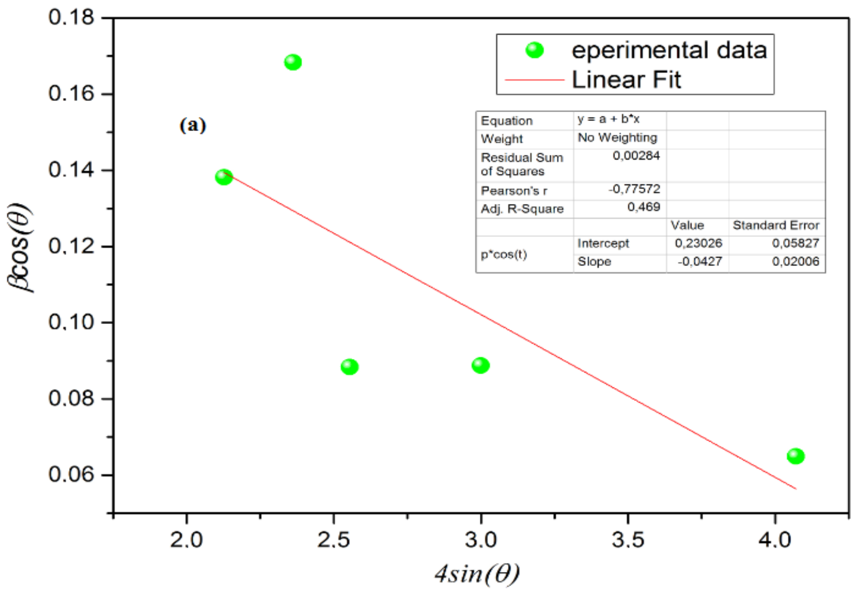

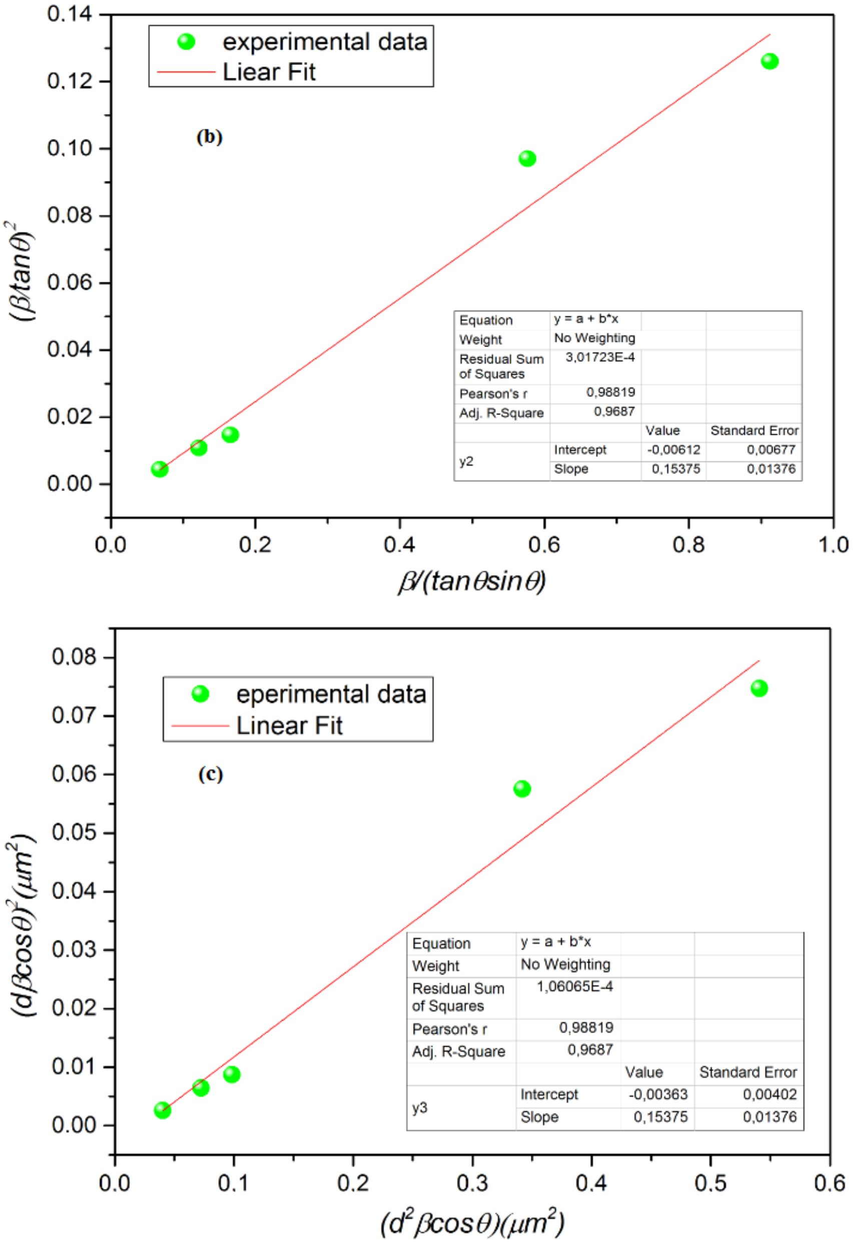

Fig.3: W-H, H-W, and SSP plot of $La_{0.7}Sr_{0.2}Na_{0.1}MnO_3$ ceramic

Methods	D-S and Wilson method		W-H plot		H-W plot		SSP technique	
	D_{D-S} (nm)	Strain ε_W	D_{W-H} (nm)	Strain ε_{W-H}	D_{H-W} (nm)	Strain ε_{H-W}	D_{SSP} (nm)	Strain ε_{SSP}
	42	$1.2.10^{-3}$	37	$3.4.10^{-3}$	20	$1.7.10^{-3}$	24	$2.2.10^{-3}$

Table 2: estimated value of Crystallite size and lattice strain using Size-strain plot, Debye-Scherrer, Halder-Wagner, and Williamson-Hall method.

3.3 ELECTRICAL ANALYSIS

To further explore the electrical transport properties of the $La_{0.7}Sr_{0.2}Na_{0.1}MnO_3$ compound and to evaluate its application as electrode material for supercapacitors due to its high electrical conductivity and dielectric constant, the progression of dc-conductivity versus temperature is illustrated in **Fig.4.a.** The temperature dependence of the electrical conductivity of $La_{0.7}Sr_{0.2}Na_{0.1}MnO_3$ indicates that the material reveals a typical semiconductor behavior over the completely explored temperature range [200K-360K]. Such behavior can be explained by the increase of the Na content that prevents the metallic phase and reduces the metal-semiconductor transition $T_{M\text{-}SC}$ that is strongly dependent on Mn^{3+}/Mn^{4+} content, structural parameters, doping site, and grain boundary defects **[33]**. Fan et al. **[34]** studied the effect of Sm, Dy, and Er-doping at the A-site of $La_{0.6}A_{0.1}Sr_{0.3}MnO_3$. They confirmed that the transition temperature is proportional to the A site average cationic radius. Moreover, Baaziz et al. **[35]** claim that the $T_{M\text{-}SC}$ of the $La_{0.67}Sr_{0.33}MnO_3$ sample was estimated to be 160 K and suggest that conductivity can be attributed to the disordered surface explained by the grain size effect and the core-shell mechanism. When increasing temperature, the rise of dc-conductivity is attributed to the enhancement of thermal energy and the charge-carriers hopping motion involved in the conduction. Indeed, the interaction between electron and lattice produced a strong electron-phonon coupling in the system rise to the formation of small polaron and the configuration of the thermally activated transport at high temperatures. Such a result is assumed to originate from the Zener double exchange process in the compound. Despite the steric effects and the weakness of the double-exchange interaction originating from the incorporation of Na^+ cation into the structure **[36, 37]**, the electrical conductivity with a value of 0.043 $S.cm^{-1}$ was still significantly high at room temperature. This value can be compared favorably with other compounds and conductivities of pure Silicon (1.67×10^{-2} to 10 $S.cm^{-1}$) for energy conversion devices, especially Solid oxide fuel cells **[38, 39]**.

A quantitative investigation of the experimental data was applied to analyze the strong temperature dependence of the charge dynamics based on the small polaron hopping (SPH) and variable range hopping (VRH) model **[40]**. At the temperature range $\theta_D/4 \ll T \ll \theta_D/2$ where $\theta_D = 520\ K$ denotes the Debye temperature, the dc-conductivity (σ_{dc}) follows the framework of Greaves-VRH approximations associated to a considerable interaction between charges. This model was successfully performed by Greaves **[41]** to describe the dc-conductivity using the relation**:**

$$\sigma_{dc}T^{1/2} = A.\exp\left(-B/_{T^{1/4}}\right) \quad \textbf{(16)}$$

$$B = (T'_0)^{1/4} = 2.1[\alpha^3/k_B.N(E_F)]^{1/4} \quad \textbf{(17)}$$

Where T'_0 denotes a constant. To prove the accuracy of the Greaves-VRH mechanism in the description of σ_{dc}, we plotted the curve of ln ($\sigma_{dc}.T^{1/2}$) versus $T^{-1/4}$. The linearity behavior of this curve confirms that Greaves-VRH is the appropriate mechanism for studying the transport properties and estimating the T'_0 value using linear fit as shown in **Fig.4.b**. The aforementioned investigation and the validity of this model prove that our compound presents a high density, significant charge mobility, and an important short-range translational motion **[42]**. At high temperatures, the SPH model can investigate the dc-conductivity [43]. Such a model is mathematically defined using the Arrhenius law expressed $\sigma_{dc}.T = \sigma_0 \exp(-E_a / k_B.T)$ where E_a and k_B denote the activation energy and the Boltzmann constant, respectively. This model considers that small polarons are trapped in a local potential well with E_a height. The rise of temperature causes a reduction of the good effect and permits the motion of polaron to the nearest neighbor site increasing the conductivity and proving the thermal activation behavior of conduction **[44]**.

The activation energies are derived from a linear fit of dc-conductivity and the estimated value E_a= 31 meV (**inset of Fig.4.c**) can be attributed to the effect of the electrical contribution which depends highly on the structural feature**.**

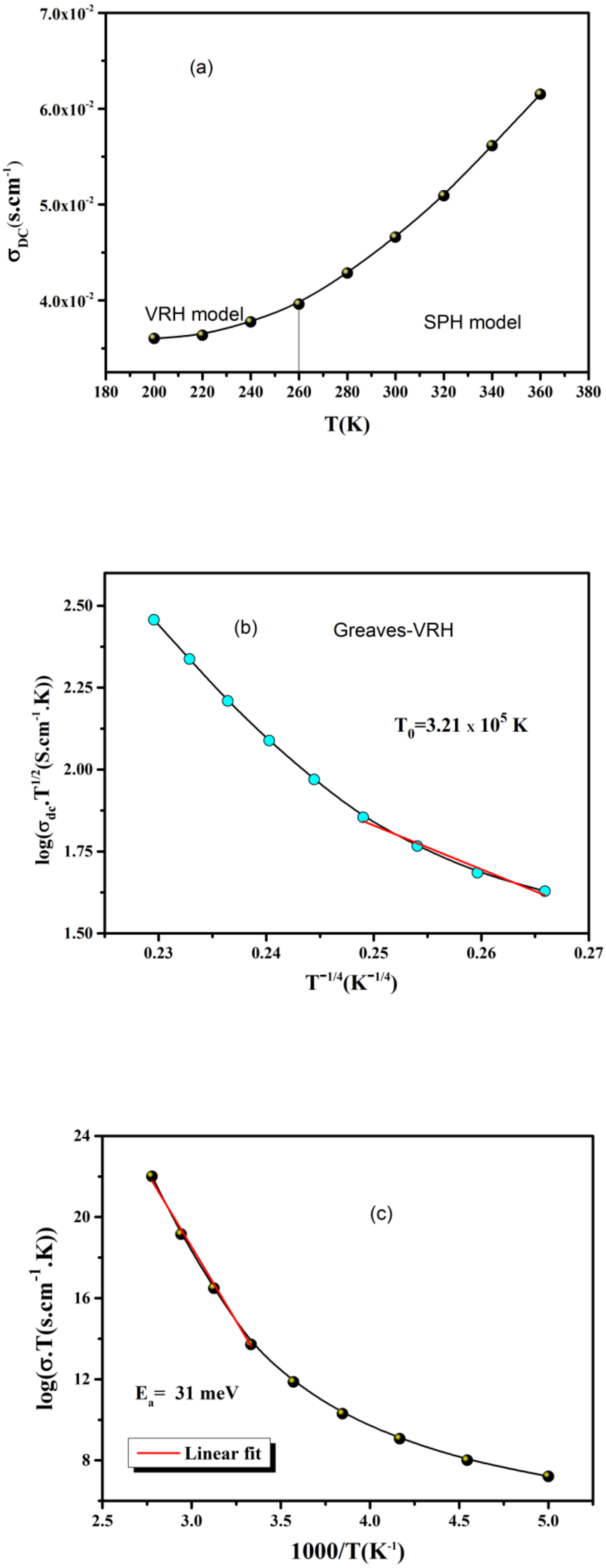

Fig.4: (a) temperature dependency of dc-conductivity for $La_{0.7}Sr_{0.2}Na_{0.1}MnO_3$ ceramic. **(b)** Variation of log(σ_{dc}.$T^{1/2}$) versus $T^{-1/4}$ and validity of Greaves-VRH model.**(c)** Plot of log (σ_{DC}.T) vs. 1000/T

Fig.5.a presents the variation of electrical conductivity the frequency at various measuring temperatures ranging from 200 to 360 K. At low frequencies, each spectrum shows a frequency-independent plateau region σ_{DC} (dc-conductivity). Such plateau is attributed to the long-range translational motion of the charge carriers **[45]**. It is worth noticing that the charge carrier hopping process can explain a high-frequency dispersion region referring to an exponential rise of conductivity. For the studied system, the frequency dependence of the electrical conductivity is proportional to the applied electric field. In this study, the frequency and temperature dependences on the electrical conductivity reflected the presence of several electrical hopping processes. To identify the hopping dynamics of the charge carriers, the variation of the conductivity data with frequency can be well-fitted using Jonscher's universal power law expressed as follows **[46]**:

$$\sigma = \sigma_{DC} + \sigma_{AC} = \sigma_{DC} + A\omega^{n} \qquad \textbf{(18)}$$

Where A is the temperature-dependent constant and n (0< n <1) denotes the power law exponent. The exponent 'n' measures the interaction degree of the charge and its environments associated with the variation of polarizability and the hopping energy barriers of the involved compound **[47]**. It is worth noticing that the electrical conductivity showed a linear behavior at high frequencies, which provides a single conduction process explained by the short-range hopping model. **Fig.5.b** presents the variation of the exponent 'n' versus temperature estimated by a linear fitting of electrical conductivity at high frequency. It was observed that the frequency exponent 'n' decreases gradually as the temperature rises, which directly highlights the activation of the Correlated Barrier Hopping (CBH) conduction process overpowered by the short-range thermally activated energy **[48]**. This behavior proves that electrical conductivity is thermally activated and the dynamic region of the spectra is influenced by the higher mobility of the electrons/polarons and hopping pathways. The presence of the CBH process suggests that single-polaron and bi-polaron hopping govern the transport behavior processes. In this case, the temperature dependence of the frequency exponent n can be expressed using the following equation **[49]**:

$$n = 1 - \frac{6K_BT}{W_m} \qquad \textbf{(19)}$$

W_m is the energy necessary to move an electron from one site to another known as the maximum barrier jump height. To evaluate precisely the transport process associated with CBH conduction, we plotted the variation of (1-n) value versus temperature in **Fig.5.b**. It can be inferred that the observed curve presents two zones with different activation energies estimated from the linear slope. In the current investigation, the modification in the activation energy value indicates that the microstructure variables showed a high dependence on the temperature effect of the studied manganite.

To analyze the conduction dynamics and the charge transport behavior of the compound, different models were performed to check the validity of the Time-Temperature Superposition Principle (TTSP) using the scaling behavior approach **[50]**. In this study, the conductivity isotherms can be studied using the Summerfield scaling process defined by the equation as follows **[51]**:

$$\frac{\sigma(\omega)}{\sigma_{dc}(T)} = F\left(\frac{\omega}{\sigma_{dc}T}\right) \qquad \textbf{(20)}$$

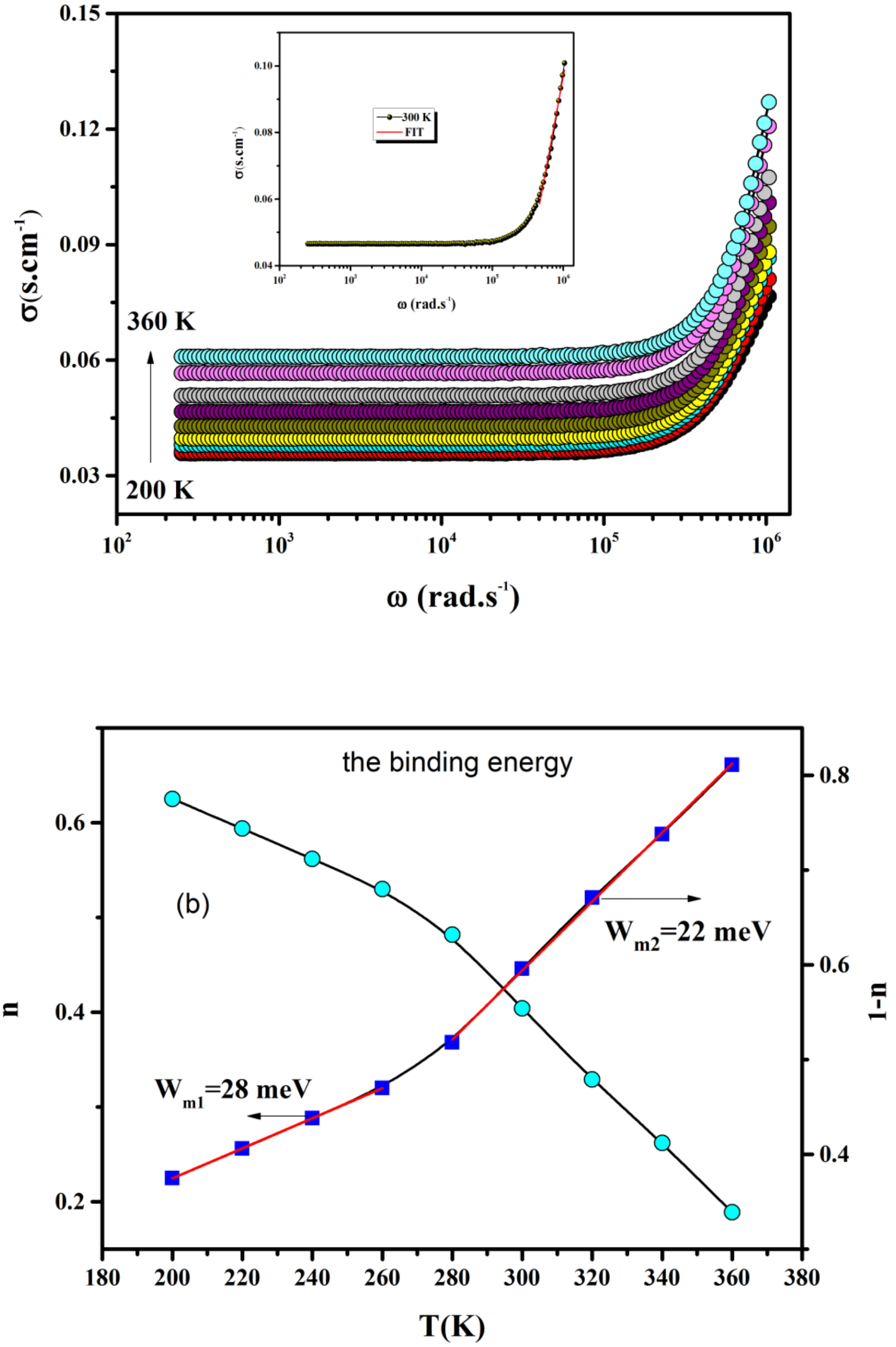

Fig.5: (a) frequency-dependent ac conductivity for $La_{0.7}Sr_{0.2}Na_{0.1}MnO_3$. Inset: The frequency dependence of ac conductivity with the linear fitting (red solid line) of conductivity obeying the simple power Law at 300 K. **(b)** Temperature dependence of frequency exponents (n) and (n-1) with temperature

Fig.6.a presents the master curve plot of the conductivity using the Summerfield scaling model. At low and intermediate frequencies, all conductivity spectra collapsed into single master curves, which indicates that the relaxation mechanism is independent of temperature and proves the validity of TTSP nature with a single electrical transport process. At high-normalized frequencies, this curve showed a deviation of the scaled spectra and confirmed the divergence feature of the conductivity. Such behaviors of the Summerfield scaling failure are attributed to the modification of the available pathways number and charge carriers density under the temperature effect **[52]**.

To ensure the best master curve, we established the modified Summerfield model expressed by the forms **[53]**:

$$\frac{\sigma(\omega)}{\sigma_{dc}(T)} = F\left(\frac{\omega}{\sigma_{dc}T}\left(\frac{T}{T_0(scale)}\right)^{\alpha}\right) \qquad \textbf{(21)}$$

This model gives valuable insights into the dominant factors that influence the dynamics of charge carriers. The scaling approach of conductivity is highly associated with the scaling exponent (α) which depends on the electric inhomogeneities. Recently, Baranovskii et al. **[54]** have analyzed the electrical conductivity using the Random Barrier Model. They confirmed that the negative value ($\alpha = -1/3$) of the scaling exponent can be attributed to the non-interacting particles. Indeed, several research groups assumed that (α) can deviate from the indicated value **[55]**. **Fig.6.b** shows the scaling behavior approach of the electrical conductivity using a modified Summerfield process and additive factor. It is worth noting that all the electrical conductivity spectra for several temperatures coalesced almost perfectly into a universal master curve using an estimated value of scaling exponent ($\alpha = 1.2$). Hence, the aforementioned behavior proves the major role of the inter-ionic Coulomb interactions the in dynamics of charge carriers' motions **[56]**.

Investigation of the dielectric properties and the origin of the high dielectric constant present an important parameter to increase the performance of the compounds that exhibits a typical behavior of tunable capacitor applications **[57, 58]**. Generally, the complex dielectric constant can be described by the expression:

$$\varepsilon^{*} = \varepsilon' + i\varepsilon'' \qquad \textbf{(22)}$$

Where (ε') and (ε'') denote the real and imaginary parts of the dielectric constant, respectively

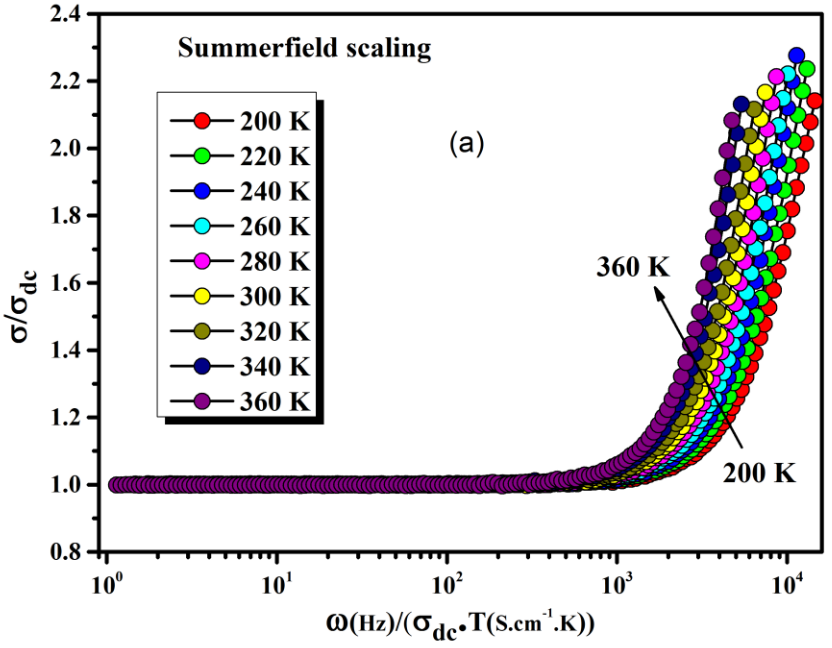

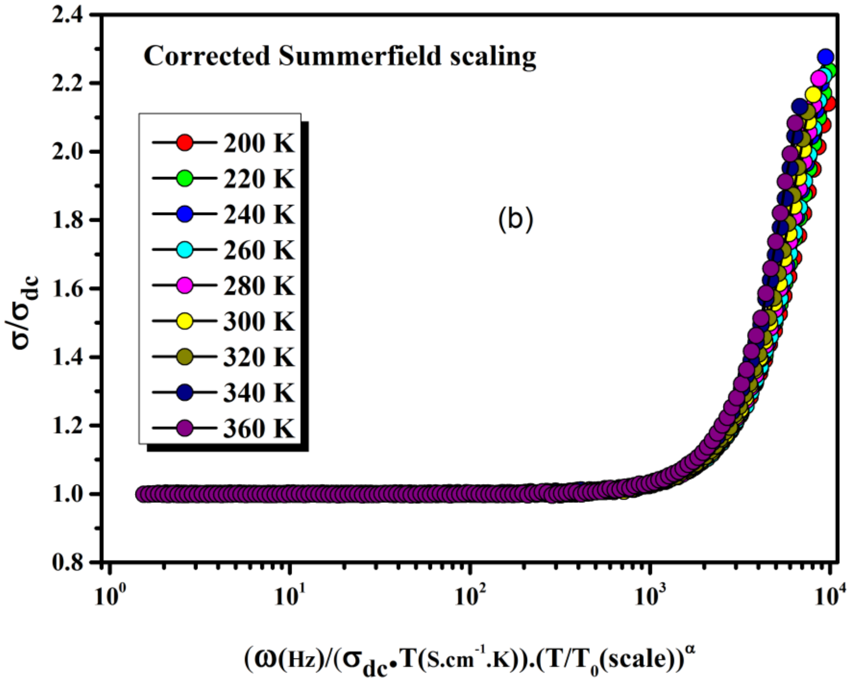

Fig.6: Super master curve of the conductivity isotherms using (a) Summerfield model and modified (b) Summerfield model.

Fig.7 presents the dependency of the imaginary part (ε") and the loss factor of dielectric constant versus frequency at several temperatures. At low frequencies, a strong dispersion feature below 1 kHz is mainly dominated by the dipolar and interfacial polarization process explained by the Maxwell-Wagner-Sillars model and Koop's phenomenological theory **[59]**. In addition, the high value of (ε") sharply decreased and merged with the rise of the frequency until reaching a constant ε_∞ at high frequencies where the electron/hole exchange remains unchanged. In fact, (ε") depends on the polarization and conduction mechanism controlled by an energy barrier between adjacent grains **[60]**. Generally, the grain boundary plays a vital function in relaxation and conductivity features at low frequency meanwhile the grains sharply take effect at high frequency. Similar behavior was observed for the dielectric loss factor (tan δ) spectra shown in the **inset of Fig.7**. In fact, the dielectric loss factor decreased significantly in the overall measured frequency range without any sign of relaxation peak for all temperatures. This proves the non-Debye relaxation behavior in the investigated material. Usually, the loss factor depends on the mobility of the charge carriers that can be affected by both grain boundary and grain resistivity values at low and high frequencies, respectively. According to Koop's theory, it is evident to relate the behavior of the dielectric loss with the energy required to exchange electrons between two Mn ions under the applied frequency **[61]**.

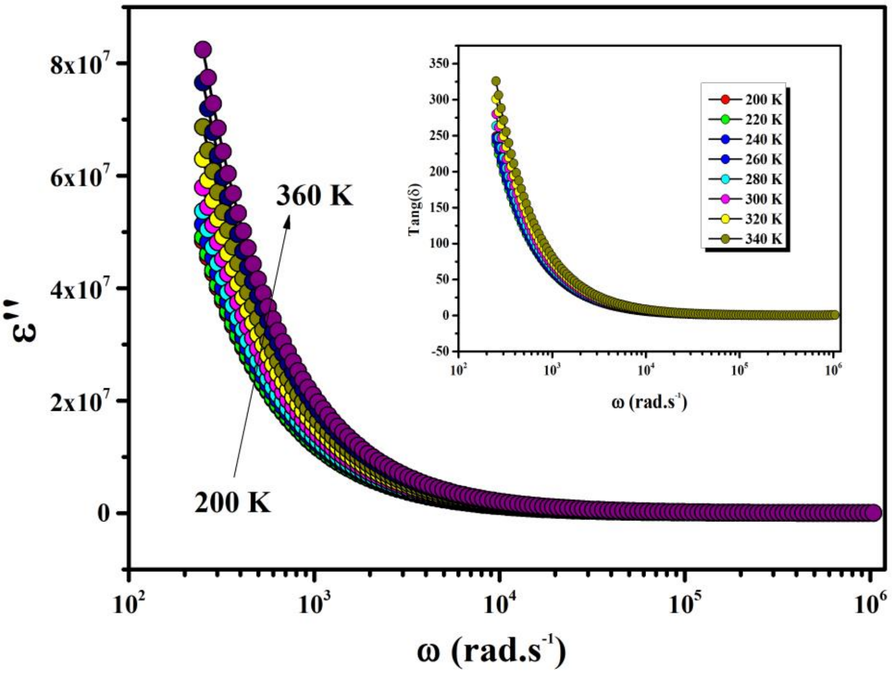

Fig.7: Frequency dependence of the imaginary part of the permittivity at different temperatures. Inset: variation of dielectric loss (tanδ) versus frequency at different.

4- Conclusion

In summary, a detailed study of the structural characteristics, conduction mechanisms, and dielectric properties of the $La_{0.7}Sr_{0.2}Na_{0.1}MnO_3$ manganite that is synthesized using a sol-gel process was systematically performed. The electrical and dielectric investigations are effectuated over large frequency and temperature ranges using the impedance spectroscopy (IS) technique. The XRD study has confirmed that the elaborated sample crystallizes in a rhombohedral distorted structure with a $R\bar{3}c$ space group. With the application of the Size-Strain method, we have found that the elaborated structure exhibits a crystallite size and lattice strain values of D_{SSP}=24 nm and ε_{SSP} =2.2.10^{-3}, respectively. From the evolution of the DC electrical conductivity versus the temperature, we have found that the studied material exhibits a semiconductor nature that is attributed to the contribution of the hopping conduction processes (VRH, and SPH). In the limit of the AC regime, our investigation proves that the CBH model is appropriate to study the conduction phenomena in the elaborated compound. After the application of the scaling laws, the obtained conductivity spectra confirm the validity of the time-temperature superposition principle. The Summerfield scaling deviations are explained by the Coulomb interaction effect. It has also been found the interfacial polarization process and Koop's theory that is due to the presence of double layers effect into the material mainly describes the high dielectric constant of the material. The high electrical conductivity and the elevated dielectric constant make the studied manganite attractive for energy industry applications such as cathode materials.

REFERENCES

[1] Luderer, G., Madeddu, S., Merfort, L. et al. Impact of declining renewable energy costs on electrification in low-emission scenarios. Nat Energy 7, 32–42 (2022).
[2] Fei Yan, Kaiwei Huang, Tao Jiang, Xiaofeng Zhou, Yunjing Shi, Guanglong Ge, Bo Shen, Jiwei Zhai, Significantly enhanced energy storage density and efficiency of BNT-based perovskite ceramics via A-site defect engineering, Energy Storage Materials. 30 (2020) 392-400
[3] S.EL. Kossi, Ch. Rayssi, AH. Dhahri, J. Dhahri, K. Khirouni, High dielectric constant and relaxor behavior in $La_{0.7}Sr_{0.25}Na_{0.05}Mn_{0.8}Ti_{0.2}O_3$ manganite, Journal of Alloys and Compounds 767 (2018) 456-463,
[4] Qiong Wu, XingHao Chen, Lei Zhao, YueShun Zhao, YunPeng Zhou, Shifeng Zhao, The relaxor properties and energy storage performance of Aurivillius compounds with different number of perovskite-like layers, Journal of Alloys and Compounds,911 (2022) 165081
[5] Peng Yuan, Haoran Xu, Zeyu Ning, Gang Xiao, Understanding thermochemical energy storage performance of $Ba_{1-x}Sr_xCoO_{3-\delta}$ perovskite system: A computational and experimental study, Journal of Energy Storage 61 (2023) 106695
[6] Prakash Ramakrishnan, Jae-won Lee, Seong-Ho Baek, The oxygen electrode bifunctionality studies: La_2FeNiO_6 double perovskite nanoparticles, Journal of Alloys and Compounds 918 (2022) 165492
[7] Isacfranklin Melkiyur, Yuvakkumar Rathinam, P. Senthil Kumar, Asaithambi Sankaiya, Selvakumar Pitchaiya, Ravi Ganesan, Dhayalan Velauthapillai. A comprehensive review on novel quaternary metal oxide and sulphide electrode materials for supercapacitor: Origin, fundamentals, present perspectives and future aspects, Renewable and Sustainable Energy Reviews 173 (2023) 113106
[8] Kashif Khan, Zaheer uD Din Babar, Sana Qayyum, Muhammad Bilal Hanif, Sajid Rauf, Amir Sultan, Michał Mosiałek, Martin Motola, Bin Lin, Design of efficient and durable symmetrical protonic ceramic fuel cells at intermediate temperatures via B-site doping of Ni in $BaCe_{0.56}Zr_{0.2}Ni_{0.04}Y_{0.2}O_{3-\delta}$, Ceramics International, 49 (2023) 16826-16835
[9] Reza Peymanfar, Shahrzad Javanshir, Preparation and characterization of $Ba_{0.2}Sr_{0.2}La_{0.6}MnO_3$ nanoparticles and investigation of size & shape effect on microwave absorption, Journal of Magnetism and Magnetic Materials 432 (2017) 444-449
[10] Y. Moualhi, R. M'nassri, Muaffaq M. Nofal, H. Rahmouni, A. Selmi, M. Gassoumi, N. Chniba-Boudjada, K. Khirouni, A. Cheikrouhou, Influence of Fe doping on physical properties of charge ordered praseodymium-calcium-manganite material, European Physical Journal Plus, 2020, 135, 809.
[11] S. EL.Kossi, S. Ghodhbane, S. Mnefgui, J. Dhahri, E. K. Hlil, The impact of disorder on magnetocaloric properties in Ti-doped manganites of $La_{0.7}Sr_{0.25}Na_{0.05}Mn_{(1-x)}Ti_xO_3$ ($0 \leq x \leq 0.2$), Journal of Magnetism and Magnetic Materials 395 (2015) 134-142.
[12] P. Muhammed Shafi, Debananda Mohapatra, V. Pradeep Reddy, Ganesh Dhakal, Deivasigamani Ranjith Kumar, Dirk Tuma, Thierry Brousse, Jae-Jin Shim, Sr- and Fe-substituted $LaMnO_3$ Perovskite: Fundamental insight and possible use in asymmetric hybrid supercapacitor, Energy Storage Materials 45 (2022) 119-129
[13] Lang, Xueqin and Mo, Haiyang and Hu, Xiaoying and Tian, Hongwei. Supercapacitor performance of perovskite $La_{1-x}Sr_xMnO_3$ Dalton Trans., ,46 (2017) 13720-13730
[14] Y. Q. Wang, Ian Maclaren, X. F. Duan, Z. H. Wang, B. G. Shen. Effect of A-site cation size mismatch on charge ordering behavior in $(La_{1-x}Y_x)_{0.5}(Ca_{1-y}Sr_y)_{0.5}MnO_3$ Journal of Applied Physics 90 (2001) 488–492
[15] Liyan Liu, Yanmei Liu, Jipeng Miao, Zhe Lü, Xianjie Wang, Yu Sui, Zhiguo Liu, Yu Li, Qingtao Huang, Degang Shang, Wenhui Su. Magnetic properties and colossal magnetoresistance of $La_{5/6}Na_{1/6}Mn_{1-y}Fe_yO_3$ with $0 \leq y \leq 0.10$, Journal of Alloys and Compounds, 427 (2007) 11-14
[16] B. Biswas, R. Nag, S. Mondal, M.H. Khan, M. Debnath, S. Taran, Sudipta Pal, Magnetic field dependent metal insulator transition by monovalent doping (Na^+) in $PrMnO_3$: Investigation through structural, magnetic and transport properties. Physica B: Condensed Matter 652 (2023) 414664
[17] H.M. Rietveld, A profile refinement method for nuclear and magnetic structures, J. Appl. Crystallogr. 2 (1969) 65-71.
[18] S. Elkossi, M. Selmi, F. Bourguiba, T. Alshahrani, H. Belmabrouk, Jamel A.S. Smida, Colossal dielectric response and non-Debye relaxation of $La_{0.7}Sr_{0.25}Na_{0.05}Mn_{0.85}Ti_{0.15}O_3$ ceramic, Inorganic Chemistry Communications 153 (2023) 110761
[19] I.I. Makoed, N.A. Liedienov, Hao Zhao, G.G. Levchenko, A.A. Amirov, G.S. Rymski, A.M. Zhivulko, K.I. Yanushkevich, Influence of rare-earth doping on the structural and magnetic properties of orthoferrite $La_{0.50}R_{0.50}FeO_3$ ceramics obtained under high pressure, Journal of Physics and Chemistry of Solids 170 (2022) 110926
[20] Xiangyu Kong, Jilin Wang, Zhengguang Zou, Fei Long, Yi Wu. Effect of Sodium Doping on Magnetic and Magnetocaloric Properties of $La_{0.65}Sr_{0.35}MnO_3$ Manganites. J Supercond Nov Magn 31 (2018) 373–379
[21] Hangfu Yang, Qiong Wu, Nengjun Yu, Yundan Yu, Minxiang Pan, Pengyue Zhang, Hongliang Ge, Study of magnetic and magnetocaloric effect of $Pr_{0.5}Sr_{0.5-x}Na_xMnO_3$ manganites. Journal of Solid State Chemistry 282 (2020) 121072
[22] Jerbi, A., Krichene, A., Thaljaoui, R., Boujelben, W.: Structural, magnetic, and electrical study of polycrystalline $Pr_{0.55}Sr_{0.45-x}Na_xMnO_3$ ($x = 0.05$ and 0.1). J. Supercond. Nov. Magn. 29(1), 123–132 (2015).

[23] Mukesh Kumar Verma, Narayan Dutt Sharma, Suman Sharma, Nisha Choudhary, Devinder Singh. High magnetoresistance in $La_{0.5}Nd_{0.15}Ca_{0.25}A_{0.1}MnO_3$ (A = Ca, Li, Na, K) CMR manganites: Correlation between their magnetic and electrical properties, Materials Research Bulletin, 125 (2020) 110813

[24] V. Goldschmidt, Geochemistry, Oxford University Press, London (1958)

[25] R. D. Shanon Crystal Physics, Diffraction, Theoretical and General Crystallography, Acta Crystallographica Section A. 32(1976) 751

[26] H. Salhi, Y. Moualhi, A. Mleiki, H. Rahmouni, K. Khirouni, Electrical and dielectric properties of the La0.4Bi0.3Sr0.2Ba0.1MnO3 ceramic synthesized by sol-gel method, European Physical Journal Plus 2023, 138, 682.

[27] A.R. Stokes, A.J.C. Wilson, The diffraction of x rays by distorted crystal aggregates - I, Proc. Phys. Soc. 56 (1944) 174–181,

[28] H. Yadav, N. Sinha, S. Goel, B. Kumar, Eu-doped ZnO nanoparticles for dielectric, ferroelectric and piezoelectric applications, J. Alloys Compd. 689 (2016) 333-341

[29] S.K. Sen, T.C. Paul, S. Dutta, M.N. Hossain, M.N.H. Mia, XRD peak profile and optical properties analysis of Ag-doped h-MoO_3 nanorods synthesized via hydrothermal method, J. Mater. Sci. Mater. Electron. 31 (2020) 1768-1786

[30] A. Gholizadeh. X-Ray Peak Broadening Analysis in $LaMnO_{3+\delta}$ Nano-Particles with Rhombohedral Crystal Structure. Journal of Advanced Materials and Processing, 3 (2015) 71-83

[31] Sapan Kumar Sen et al 2020 Adv. Nat. Sci: Nanosci. Nanotechnol. 11 025004

[32] Munmun Basak, Md. Lutfor Rahman, Md. Farid Ahmed, Bristy Biswas, Nahid Sharmin, The use of X-ray diffraction peak profile analysis to determine the structural parameters of cobalt ferrite nanoparticles using Debye-Scherrer, Williamson-Hall, Halder-Wagner and Size-strain plot: Different precipitating agent approach, Journal of Alloys and Compounds, 895 (2022) 162694

[33] Y. Moualhi, M. A. Alamri, A. Jbeli, N. A. Althumairi, S. El Kossi, R. Ben Brahem, H. Rahmouni, Elaboration of La (Sr/Na) Mn (Ti)O_3 ceramic, structural, and morphological investigations, and contribution of direct and indirect interactions on transport properties, Ceramics International 50 (2024) 16587

[34] Fan, J., Xu, L., Zhang, X. et al. Effect of A-site average radius and cation disorder on magnetism and electronic properties in manganite $La_{0.6}A_{0.1}Sr_{0.3}MnO_3$ (A = Sm, Dy, Er). J Mater Sci 50, 2130–2137 (2015)

[35] Baaziz, H., Maaloul, N. K., Tozri, A., Rahmouni, H., Mizouri, S., Khirouni, K., & Dhahri, E. (2015). Effect of sintering temperature and grain size on the electrical transport properties of $La_{0.67}Sr_{0.33}MnO_3$ manganite. Chemical Physics Letters, 640, 77–81

[36] N. Abdelmoula, E. Dhahri, N. Fourati, L. Reversat. Monovalent effects on structural, magnetic and magnetoresistance properties in doped manganite oxides. Journal of Alloys and Compounds 365 (2004) 25–30

[37] Zhang S, Dong G, Liu Y, Li HJ, Chu KL, Pu XR, Yu XH, Liu X. Effect of Na-doping on structural, electrical, and Magnetoresistive properties of $La_{0.7}(Ag_{0.3-x}Na_x)_{0.3}MnO_3$ polycrystalline ceramics. Ceram Int 46 (2020) 584–591

[38] I. Sfifir Debbebi, S. Megdiche-Borchani, W. Cheikhrouhou-Koubaa, A. Cheikhrouhou, Study of complex impedance spectroscopic properties of La0.7-xDyxSr0.3MnO3 perovskite oxides, R. Soc. Open Sci. 5 (2018) 172201

[39] Andreja Žužić, Antonia Ressler, Ana Šantić, Jelena Macan, Andreja Gajović. The effect of synthesis method on oxygen nonstoichiometry and electrical conductivity of Sr-doped lanthanum manganites, Journal of Alloys and Compounds 907 (2022): 164456

[40] Y. Moualhi, A. Mleiki, H. Rahmouni, K. Khirouni, A. Cheikhrouhou, Temperature, frequency and bias voltage effects on the electrical transport properties of (Sm-Pr-Sr)MnO3 perovskite, Materials Research Bulletin 2022, 155, 111976.

[41] G.N. Greaves, Small polaron conduction in V_2O_5 P_2O_5 glasses, J. Non-Cryst. Solids 11 (1973) 427

[42] Y. Moualhi, H. Rahmouni, K. Khirouni. Dynamics of charge carriers in doped manganite based on conductivity measurements and theoretical models, physica B 616 (2021) 413129

[43] Liu, X., X. Xu & Y. Zhang (2000) Effect of Ti dopant on the carrier density collapse in colossal magnetoresistance material $La_{0.7}Ca_{0.3}Mn_{1-y}Ti_yO_3$. Physical Review B, 62, 15112.

[44] Dhanalakshmi, B., P. Kollu, B. P. Rao & P. S. Rao (2016) Impedance spectroscopy and dielectric properties of multiferroic $BiFeO_3/Bi_{0.95}Mn_{0.05}FeO_3$–Ni0. 5$Zn_{0.5}Fe_2O_4$ composites. Ceramics International, 42, 2186-2197

[45] Khan, A. A., M. U. Fayaz, M. N. Khan, M. Iqbal, A. Majeed, R. Bilkees, S. Mukhtar & M. Javed (2018) Investigation of charge transport mechanism in semiconducting $La_{0.5}Ca_{0.5}Mn_{0.5}Fe_{0.5}O_3$ manganite prepared by sol–gel method. Journal of Materials Science: Materials in Electronics, 29, 13577-13587.

[46] A. K. Jonscher, The ‘universal’ dielectric response, Nature 267 (1977) 673.

[47] A. Peláiz-Barranco, M. P. Gutiérrez-Amador, A.Huanosta, R.Valenzuela, Phase transitions in ferromagnetic and ferroelectric ceramics by ac measurements, Appl. Phys. Lett.73 (1998) 2039-2041.

[48] M. Das Pattanayak, L. Biswal, Karubaki Moharana, Niladri Roy Frequency and temperature dependent transport properties of sn doped $Ba_{0.5}Sr_{0.5}TiO_3$ ceramics. 2740 (2023) 040007

[49] Raddaoui, Z., El Kossi, S., Al-shahrani, T. et al. Study of structural, conduction mechanism and dielectric behavior of $La_{0.7}Sr_{0.3}Mn_{0.8}Fe_{0.2}O_3$ manganite. J Mater Sci: Mater Electron 31(2020) 21732–21746.

[50] Moualhi, Y., M’nassri, R., Nofal, M.M. et al. Magnetic properties and impedance spectroscopic analysis in $Pr_{0.7}Ca_{0.3}Mn_{0.95}Fe_{0.05}O_3$ perovskite ceramic. J Mater Sci: Mater Electron 31 (2020) 21046–21058.

[51] Pragati Singh, Pardeep K. Jha, Priyanka A. Jha, Prabhakar Singh, Influence of sintering temperature on ion dynamics of $Na_{0.5}Bi_{0.5}TiO_{3-\delta}$: Suitability as an electrolyte material for SOFC, International Journal of Hydrogen Energy 45 (2020) 17006-17016

[52] Ah. Dhahri, Y. Moualhi, C. Henchiri, A. Benali, P. Sanguino, M.P.F. Graça, M.A. Valente, N. Abdelmoula, H. Rahmouni, B.F.O. Costa, Study of structural properties and conduction mechanisms of $La_{0.67}Ca_{0.2}Ba_{0.13}Fe_{0.97}Ti_{0.03}O_3$ perovskite, Inorganic Chemistry Communications 140 (2022) 109435
[53] Y. Moualhi, M. Smari, H. Rahmouni, K. Khirouni, E. Dhahri, Superlinear dependence of the conductivity, double/single Jonscher variations and the contribution of various conduction mechanisms in transport properties of La0.5Ca0.2Ag0.3MnO3 manganite, Journal of Alloys and Compounds, 898, (2022) 162866.
[54] S.D. Baranovskii, H. Cordes, On the conduction mechanism in ionic glasses J. Chem. Phys. 111(1999) 7546
[55] A. Ghosh, A. Pan, Scaling of the conductivity spectra in ionic glasses: dependence on the structure, Phys. Rev. Lett. 84 (2000) 2188.
[56] Sevi Murugavel and Bernhard Roling J. Phys. Chem. B, 108 (2004) 2564-2567.
[57] K.X. Jin, B. Yang, Y. Zhang, B.C. Luo, L.Y. Chen, C.L. Chen, Tunable dielectric properties induced by optical fields in barium strontium titanate/manganite heterostructures, Scripta Materialia, 112 (2016) 62-66
[58] Y. Moualhi, A. Mleiki, H. Rahmouni, K. Khirouni, Investigation of the dielectric response and the transport properties of samarium and strontium-based manganite, European Physical Journal Plus 137, (2022) 406.
[59] Layla Badr , Low temperature conductivity and ion dynamics in silver iodide-silver metaphosphate glasses, Phys. Chem. Chem. Phys.,19 (2017) 21527-21531.
[60] Y. Moualhi, M. Smari, H. Nasri, H. Rahmouni, Combined experimental characterization and conduction models based on impedance spectroscopy for studying the microstructural and transport properties of electro-ceramic perovskites, Material Today communications 38 (2024) 108529.
[61] Gowreesan, S., Ruban Kumar, A. Structural, magnetic, and electrical property of nanocrystalline perovskite structure of iron manganite (FeMnO3). Appl. Phys. A 123, 689 (2017).

الملخص باللغة العربية

"خصائص العزل والتوصيلية العالية لمركب أكسيد المنجنيز اللانثانومي السترونتيومي المشوب بأيون الصوديوم لتطبيقات مواد الكاثود

رحمة عياد ابراهم
المملكة العربية السعودية، القصيم، بريدة، جامعة القصيم ،كلية العلوم، قسم الفيزياء

تم تحضير أكسيد المنجنيز La0.7Sr0.2Na0.1MnO3 ذو التوازن المختلط باستخدام طريقة صول جال(sol-gel) يتم تفصيل الخصائص الهيكلية والكهربائية والعازلة لـ La0.7Sr0.2Na0.1MnO3 عبر نطاقات درجات الحرارة والتردد الواسعة للحصول على معلومات حول ديناميكية حاملات الشحنات في هيكل منجنيت.

عند درجة حرارة الغرفة، تكشف مجموعات من قياسات تشتيت الأشعة السينية التجريبية (XRD) ونتائج الحسابات باستخدام تحليل Rietveldأن La0.7Sr0.2Na0.1MnO3 يتبلور في مرحلة نقية تنتمي إلى هيكل سداسي السطوح مع مجموعة الفضاء .$R\bar{3}c$ باستخدام تقنية الحجم - الإجهاد، تقدر أحجام البلورة وقيم الإجهاد الشبكي المقدرة بـ DSSP=24 نانومتر و3-ƐSSP =2.2.10 ،

تكشف النتائج في دراسة توصيلية التيار المستمر الكهربائي أن المادة المدروسة تظهر سلوكًا شبه موصلًا عبر نطاق درجات الحرارة المدروسة. يتم استقصاء هذا السلوك باستخدام نماذج التوصيل بالبولارون الصغير والقفز المتغير في المدى.

علاوة على ذلك، يظهر دراسة توصيلية التيار المستمر أن وجود أمتصاص كبير للشحنات وتفاعلات قوية بين الإلكترونات والفونونات تميز .La0.7Sr0.2Na0.1MnO3 بالنسبة للنظام المدروس، تكشف درجة ديباي المستنتجة عن θD=520 كلفن. تحسن وجود أيون الصوديوم في المنجنيت المدروس بشكل رئيسي قيمة توصيلية التيار المستمر الكهربائي خاصة عند حوالي درجة حرارة الغرفة التي تصل إلى σDC (300K) = 4.3 10-2

تكشف التحقيقات الكمية في التبعية لدرجة الحرارة لمعاملات التردد n (T) عند ترددات عالية أن نموذج القفز بحاجز مترابط كان الأقوى في توصيل الكهرباء في نظام التيار المتردد. يثبت المعدل التكبيري (α) صحة مبدأ التركيب الزمني للحرارة. وفقًا لنظريةKoop ، علاوة على ذلك، تشير سلوك عملاق للثابت العازل (ε") بقيمة تزيد عن 106 ووجود توصيليات كهربائية عالية بمقدار 4.3 10-2 سم-1 إلى إمكانية تطبيق هذا المركب في أجهزة تخزين الطاقة.

الكلمات المفتاحية: توصيلية الكهربائية*بيروفسكيت* ، الثابت العازل ، XRD-الأشعة السينية.